

Article

# A Multi-Physics Modeling-Based Vibration Prediction Method for Switched Reluctance Motors

Xiao Ling, Jianfeng Tao \*, Bingchu Li, Chengjin Qin  and Chengliang Liu

The State Key Laboratory of Mechanical System and Vibration, School of Mechanical Engineering, Shanghai Jiao Tong University, Shanghai 200240, China; lingxiao@sjtu.edu.cn (L.X.); bchli@sjtu.edu.cn (B.L.); qinchengjin@sjtu.edu.cn (C.Q.); chlliu@sjtu.edu.cn (C.L.)

\* Correspondence: jftao@sjtu.edu.cn; Tel.: +86-021-3420-6053

Received: 19 September 2019; Accepted: 23 October 2019; Published: 25 October 2019



**Abstract:** Currently, vibration has been one crucial factor hindering the application of switched reluctance motor (SRM). Hence, it is of crucial importance to predict and suppress this undesirable vibration. This paper proposes a multi-physics analysis-based vibration prediction approach for SRM. It consists of three modules: digital controller and drive circuit module, electromagnetic field module, and mechanical module. In the mechanical module, it not only includes the influence of the stator, but also fully considers the influence of rotor, end cover, bearing, and other components of the motor on the system modal. Moreover, the vibration data under different control strategies are obtained in real time, and data dynamic interaction between the three segments can also be achieved. By combining the electromagnetic forces and the system structure modal, the vibration of SRM can be predicted. Finally, the effectiveness of the proposed method was verified on 12/8 poles, 1.5KW SRM drive system test bench. The results demonstrate that the modal simulation method based on static pre-calculation achieves high accuracy, and the vibration spectrums predicted by the proposed method shows good agreement with the experimental results.

**Keywords:** switched reluctance motor; vibration prediction; multi-physics modelling

## 1. Introduction

Due to its simple structure, low cost and high reliability, a switched reluctance motor (SRM) has been highlighted for many industrial applications [1,2]. For instance, SRM is considered as a promising candidate for the distributed-driven electric vehicle [3,4]. Based on the analytical Fourier fitting method, Sun et al. [5] presented a convenience method for modeling an in-wheel switched reluctance motor. To alleviate the harmful effects of vibration induced by the unbalanced electromagnetic force, Qin and co-workers [6] developed a vibration mitigation method based on a dynamic vibration absorbing structure. Despite its many advantages, SRM suffers from inherent vibration and acoustic noise, which limits its application in the industrial potential market. Therefore, researchers have investigated the vibration and acoustic noise problem for SRM from various aspects: stator and rotor pole shaping [7], motor topology optimization [8,9], switching angle adjustment [10], insert of zero voltage loop during switching [11], and current waveform profiling [12]. In order to predict the vibration of SRM, accurate modal analysis and radial force calculation are of vital significance.

The natural frequencies and vibration modes of SRM can be calculated by modal analysis, which are used to analyze the vibration characteristics. Cai et al. [13] showed that the vibration is largest when the harmonic frequency of electromagnetic force coincides with the modal frequency. Callegaro et al. [14] recommended a phase radial force shaping method based on harmonic content analysis, which was experimentally validated with experiments at different speed and load conditions. Kimpara and co-workers [15] analyzed the mechanical coupling path of stator and rotor and its

influence on vibration modes. Taking into account the electromagnetic characteristics, mechanical vibration, and acoustic noise, Liang et al. [16] proposed a numerical modeling method for classical SRM and mutually coupled SRM. In [17], FEA methods were used to determine the modal shapes and natural frequencies for SRM, and the influence of end-bell and self-weight were also considered. However, the above methods only analyzed the modal of the motor stator, and did not consider the influence of windings, end cover, bearings, and other components on the system modal. Radial electromagnetic force is the main excitation source for the vibration and noise of SRM [18]. Calculation of electromagnetic force can be categorized into analytical methods and finite element analysis (FEA) methods. Anwar et al. [19] and Husain et al. [20] derived the electromagnetic field distribution of SRM by dimension parameters and calculated the radial force according to the virtual displacement principle. However, the analytical methods require precise system parameters, and the corresponding derivation process of the radial force is quite complicated. In [21,22], the finite element-based multi-physics analysis method was adopted to calculate the electromagnetic force, and the electromagnetic force was used as the excitation of the vibration model. Fiedler et al. [23] and Srivas et al. [24] proposed a multi-physical field numerical simulation method, in which only the vibration characteristics of the stator were considered.

With the obtained electromagnetic force and modal information, the vibration of the motor can be determined quantitatively. By utilizing the modal information and electromagnetic force, Fiedler et al. [23] calculated the stator vibration response by a modal superposition method. Tang and co-workers [25] established the transfer function model of vibration based on impulse excitation experiment and employed the transfer function model to calculate and analyze the vibration. Anwar et al. [19] and Lin et al. [26] computed the SRM vibration by convolution method. When the number of switching actions in a cycle is relatively large, the computational time will also increase. With the aid of a piecewise first-order linear function, Guo et al. [27] proposed an efficient vibration calculation method. However, the saturation effect is not taken into consideration.

In-depth analysis shows that the above vibration prediction methods only analyzed the vibration characteristics of the stator and ignored the influence of other components on the system vibration. To predict its vibration more accurately, it is necessary to consider the influence of more components including stator, rotor, housing winding, end cover, and bearing on the system modal. Consequently, this paper proposes a novel vibration prediction method for SRM based on multi-physics modeling. It includes three core segments: control algorithm integration, electromagnetic field dynamic analysis, electromagnetic force calculation, and modal analysis. The highlight of the proposed method is that it allows modification of system inputs, such as geometry dimensions, material parameters, or control strategies, at each step of the simulation process. The vibration data under different control strategies is obtained in real time, and data dynamic interaction between the three segments can be also achieved. Therefore, from the perspective of reducing vibration, it can be used to optimize the structural design and the control strategy of the switched reluctance motor. In addition, in the mechanical module, it not only includes the influence of the stator, but also fully considers the influence of rotor, end cover, bearing, and other components of the motor on the system modal. The remainder of this paper is organized as follows. In Section 2, the operational principle and the origin of vibration of the SRM are presented. Section 3 develops the multi-physics modeling-based vibration prediction method. In Section 4, the implementation of the prediction model is presented, and experiments are conducted to validate the proposed method. Finally, the conclusions are drawn in Section 5.

## 2. Vibration of the Switched Reluctance Motor

SRM mainly consists of a stator unit, a rotor unit and corresponding structural components, as shown in Figure 1a. The stator unit includes iron core, winding, slot wedge, insulating material and motor lead, while the rotor unit contains rotor shaft and rotor core. Both the stator and the rotor use a salient pole structure that was formed by laminating silicon steel sheets. In addition, the windings are installed only at the stator pole. Furthermore, the structural components are mainly composed of

housing, end cover, bearing cover, bearing, junction box, and junction column. Figure 1b illustrates the stator and rotor structure for a 12-8 SRM. Four radial relative windings at the stator pole form a phase. If current is applied to a specific phase of the motor (e.g., phase A), the magnetic field force is generated due to the distortion of the electromagnetic field, which makes the rotor rotate to the position where the pole axis of the rotor and the pole axis of the stator coincide. At this time, the magnetic resistance is at a minimum. When the phases B, C, A and B in Figure 1b are sequentially energized, the rotor will continuously rotate in a counterclockwise direction, and, vice versa, in a clockwise direction.

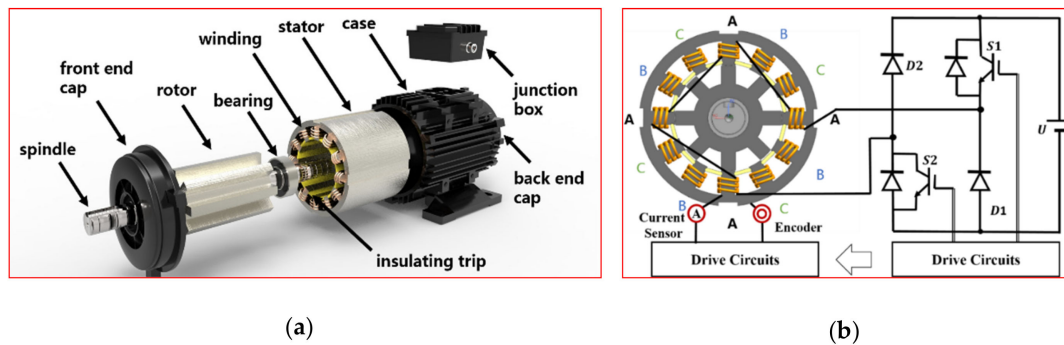


**Figure 1.** Structure and working principle of switched reluctance motor (SRM): (a) structure of SRM; (b) working principle of a 12-8 SRM.

Currently, the vibration problem is one of the research hotspots of the SRM. It is mainly caused by the change of the electromagnetic force between air gap magnetic fields of the stator and rotor. When the stator winding of SRM is energized, an induced magnetic field is formed at the stator pole, which further magnetizes the rotor. At this time, electromagnetic forces are generated between the stator and rotor, as shown in Figure 2. The electromagnetic forces acting on the stator and rotor, namely  $F_s$  and  $F_r$ , are a pair of forces and reaction forces. The electromagnetic force  $F_s$  can be decomposed into tangential magnetic force  $F_{st}$  and radial magnetic force  $F_{sr}$ . When the stator winding is excited, the radial magnetic force  $F_{sr}$  increases, stretching the stator along the radial direction. However, if the current is cut, the radial magnetic force  $F_{sr}$  is reduced to zero, and the stator rebounds in the radial direction. With the continuous commutation of the excitation winding for the SRM, the radial magnetic force  $F_{sr}$  of the different phases repeatedly attracts and releases the stator, causing structural deformation of the motor stator. If the frequency of  $F_{sr}$  is close to the natural frequency of the motor, it will excite the resonance of the motor body and cause strong radial vibration. Similarly, the electromagnetic force  $F_r$  can be also decomposed into tangential magnetic force  $F_{rt}$  and radial magnetic force  $F_{rr}$ . Due to the doubly salient construction and fundamental excitation principles, the majority of the flux in SRM is in the radial direction. Although the torque ripple caused by fluctuations of  $F_{rt}$  during motor excitation and demagnetization may also induce tangential vibration, it can be neglected compared with radial vibration, which has been also verified by the works of several researchers [1,18,26]. For instance, Cameron et al. [18] designed a series of experiments to investigate the vibration in SRM, and the experimental results showed that radial vibration of the stator frame caused by radial electromagnetic forces is the dominant source of vibration in SRM. The authors in [1,26] also proved that the acceleration response of SRM mainly resulted from the sudden change of radial electromagnetic forces. Consequently, this paper focuses on the establishment of a radial vibration prediction model.

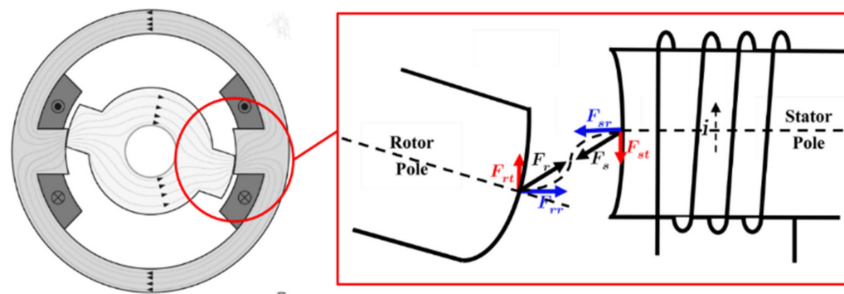


Figure 2. Schematic diagram of an electromagnetic field and electromagnetic force.

### 3. The Proposed Multi-Physics Modelling-Based Method

The operation of an SRM is a process of interaction of electro-magnetic-mechanical multiple physical fields. The performance parameters of multiple physical fields are constrained by each other. The electromagnetic characteristics of traditional motors are usually linear or quasi linear. For SRM, it has poles both on stator and rotator, and the windings are bounded on the stator, as shown in Figure 1. On the other hand, due to the saturation characteristics of ferromagnetic material, the flux linkage begins to saturate when the current reaches certain values. During the motor running process, the SRM’s electromagnetic properties versus position and phase current exhibit nonlinear characteristics and thus are difficult to model accurately compared with traditional motors. Due to its nonlinear electromagnetic characteristics and the special action mode of electromagnetic force, the multi-physics interaction behavior of SRMs is more complicated than that of traditional motors. In addition, the components of SRM, including stator, rotor, shell winding, end cover and bearing, have influence on the system modal. Therefore, for the performance optimization and control method design of SRM, it is of vital importance to model and analyze from the perspective of multi-physics field, and fully take into account the influence of more components on the system modal. This paper presents a numerical simulation method that fully considers the interaction relationship of multi-physical fields. It includes three segments: digital controller and drive circuit module, magnetic field module, and mechanical module. To obtain an excitation current, the gate signals of the controller module are employed to drive the power amplifier. The winding of SRM is energized by the generating current, and an induced magnetic field will be formed. Thereafter, the electromagnetic forces can be acquired. Finally, the vibration of SRM is predicted by combining the electromagnetic forces and the system structure modal.

#### 3.1. The Controller and Drive Circuit Models

As shown in Figure 3, the modeling of SRM controller is divided into four parts: speed controller, current controller, position and speed calculation module, and execution angle calculation module. The speed controller outputs the reference current  $I_{ref}$ , while the current controller generates a gate signal  $G_i$  that controls the interruption of insulated gate bipolar translator (IGBT). In addition, the position and speed calculation module compute the rotor angle  $\theta_{est}$  and speed  $\omega_{est}$ , while the execution angle calculation module obtains the turn on and turn off angles, i.e.,  $\theta_{on}$  and  $\theta_{off}$ . For SRMs, the modeling of the drive circuit mainly involves the modeling of the switching device IGBT. If the change of the capacitance parameter and the switching process characteristics are ignored, the saturation voltage  $V_{sat}$  and the current  $I_{sat}$  can be calculated as follows:

$$\begin{cases} V_{sat} = A_{FET} \times (V_{GS} - V_P)^{M_{FET}} \\ I_{sat} = \frac{k}{2} \times (V_{GS} - V_P)^{N_{FET}} \end{cases}, \quad (1)$$

where  $A_{FET}$  is the saturation factor,  $V_{GS}$  is the gate to source voltage,  $V_p$  is the pinch-off voltage,  $M_{FET}$  is the saturation exponent,  $N_{FET}$  is the transfer characteristic exponent, and  $k$  is the transfer constant. Meanwhile, the current  $I_C$  of the linear region is expressed as:

$$I_C = B_N \times I_{sat} \times (1 + KLM \times V_{DS}) \times (2 - \frac{V_{DS}}{V_{sat}}) \times \frac{V_{DS}}{V_{sat}}, \tag{2}$$

where  $B_N$  is gain of current, the  $KLM$  is the channel length modulation factor, and  $V_{DS}$  is the drain to source voltage. The coefficient  $k$ , the voltage  $V_p$ , and the current gain  $B_N$  are parameters that vary with temperature and can be corrected based on the actual temperature value.

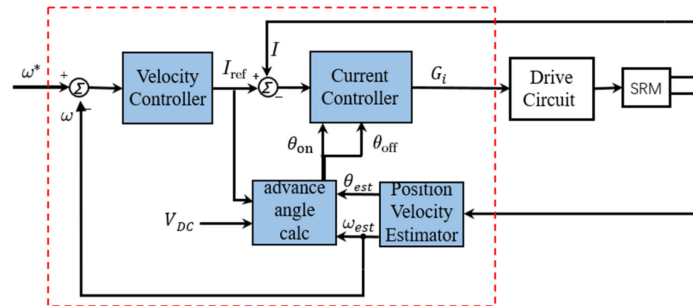


Figure 3. Controller of SRM.

### 3.2. The Electromagnetic Module

There are three main numerical methods available for the electromagnetic field simulation, including the finite element methods, boundary element methods, and finite difference methods. In this work, we adopt the most widely used finite element method based on the following assumptions [28]:

1. Neglect both magnetic flux leakages from the excitation pole to the stator yoke through the stator pole space and from the excitation pole to the adjacent stator teeth.
2. The eddy current effect is negligible.
3. Neglect the magnetic field and motor end effect outside the boundary formed between the outer diameters of stator and rotor.
4. The equation  $B_s = \nabla \times U$  is satisfied when the vector magnetic potential  $U$  is introduced in the solution domain.

Considering the above assumptions, the electromagnetic field problem in the plane  $\Omega$  can be expressed as the following boundary value problem [29]:

$$\begin{cases} \Omega : \frac{\partial}{\partial x}(\gamma \frac{\partial U_z}{\partial x}) + \frac{\partial}{\partial y}(\gamma \frac{\partial U_z}{\partial y}) = -J_z \\ \Gamma_1 : U_z = U_0 \\ \Gamma_2 : \gamma \frac{\partial U_z}{\partial n} = -H_t \end{cases}, \tag{3}$$

where  $\gamma$  is the magnetoresistance of the stator and rotor cores,  $J_z$  is the current density,  $U_z$  is the vector magnetic potential,  $H_t$  is the tangential component of the magnetic field, and  $\Gamma_1$  and  $\Gamma_2$  are the first and second boundary conditions, respectively. Equation (3) can be equivalent to a problem of the conditional variation as follows:

$$\begin{cases} W(U_z) = \iint_{\Omega} (\int_0^{B_s} \gamma B_s dB_s - J_z U_z) dx dy - \int_{\Gamma_2} (-H_t) U_z dl = \min \\ B_s = \sqrt{B_{sx}^2 + B_{sy}^2} = \sqrt{(\frac{\partial U_z}{\partial x})^2 + (\frac{\partial U_z}{\partial y})^2} \\ \Gamma_1 : U_z = U_0 \end{cases} \tag{4}$$

After a finite element division of the entire solution domain of the electromagnetic field, the difference function for each small element can be given by:

$$U = N_i U_i + N_j U_j + N_m U_m, \tag{5}$$

where  $\mathbf{U}$  is the magnetic vector potential at any point in the element,  $N_i, N_j$ , and  $N_m$  are the shape functions that are related to the element node coordinates;  $U_i, U_j$ , and,  $U_m$  are the magnetic vector potentials on the element nodes.

The algebraic equations of the nodal function can be obtained through converting the variational problem to another problem of finding the extremum of the energy function  $W$ . We can get the nodal magnetic potential by solving the algebraic equations using the Newton–Raphson method. Then, the field quantity can be obtained by a finite element post-processing. According to [30], the flux linkage  $\psi$  and inductance  $L$  through the phase winding can be expressed as

$$\begin{cases} \psi = l_{st} \int_{x_r}^{x_l} B_{sy} dx = l_{st}(U_r - U_l) \\ L = \frac{\psi}{i} = \frac{l_{st}(U_r - U_l)}{i} \end{cases} \tag{6}$$

where  $l_{st}$  is the axial length of the motor stator.  $U_r$  and  $U_l$  represent the magnetic vector potentials on the left and right sides of the coil, respectively. The radial force  $F_r$  and tangential force  $F_t$  are calculated by Maxwell tensor method as follows:

$$\begin{cases} F_r = \frac{1}{2\mu_0} \oint_S (B_{sr}^2 - B_{st}^2) dS = \frac{1}{2\mu_0} \frac{D}{2} l_{st} \sum_{i=1}^n [(B_{sri}^2 - B_{sti}^2)(\theta_i - \theta_{i-1})] \\ F_t = \frac{1}{\mu_0} \oint_S (B_{sr} B_{st}) dS = \frac{1}{\mu_0} \frac{D}{2} l_{st} \sum_{i=1}^n [(B_{sri} B_{sti})(\theta_i - \theta_{i-1})] \end{cases}, \tag{7}$$

where  $D$  is the arc length of the integral path,  $N$  is the number of arc segments,  $B_{sri}$  and  $B_{sti}$  are the radial and tangential components of flux density  $\mathbf{B}_s$ ,  $\mu_0$  is the permeability of vacuum, and  $(\theta_i - \theta_{i-1})$  is the radian angle of each arc. Finally, the electromagnetic torque  $T_e$  can be calculated by the tangential force  $F_t$  [30]:

$$T_e = \frac{D}{2} 2p F_t = \frac{l_{st} D^2}{\mu_0 4} 2p \sum_{i=1}^n [(B_{sri} B_{sti})(\theta_i - \theta_{i-1})], \tag{8}$$

where  $p$  is the number of motor rotors.

### 3.3. The Mechanical Module

The mechanical module includes two sub-modules: modal identification and vibration prediction. The modal identification integrates the constrained modal simulation and takes into account the effects of stator, rotor, shell winding, end cover, bearing, gravity, and assembly stress on the stiffness of the installed motor. The modal simulation of SRM is developed based on static pre-calculation, and the dynamic equilibrium equation of its vibration system can be given by

$$\left( \begin{pmatrix} K_{ff} & K_{fr} \\ K_{rf} & K_{rr} \end{pmatrix}_{n \times n} + \begin{pmatrix} S_{ff} & S_{fr} \\ S_{rf} & S_{rr} \end{pmatrix}_{n \times n} - \omega^2 \begin{pmatrix} M_{ff} & M_{fr} \\ M_{rf} & M_{rr} \end{pmatrix}_{n \times n} \right) \begin{pmatrix} \{u_f\} \\ 0 \end{pmatrix}_{n \times 1} = \begin{pmatrix} 0 \\ \{R_r\} \end{pmatrix}_{n \times 1}, \tag{9}$$

where  $\begin{pmatrix} K_{ff} & K_{fr} \\ K_{rf} & K_{rr} \end{pmatrix}_{n \times n}$  is the prestress matrix,  $\begin{pmatrix} S_{ff} & S_{fr} \\ S_{rf} & S_{rr} \end{pmatrix}_{n \times n}$  is the stress stiffening matrix,  $\begin{pmatrix} M_{ff} & M_{fr} \\ M_{rf} & M_{rr} \end{pmatrix}_{n \times n}$  is the mass matrix, and  $R_r$  is the binding force vector. The characteristic equation in Equation (9) can be expressed as

$$(K_{ff} + S_{ff} - \omega^2 M_{ff}) \{u_f\} = 0 \tag{10}$$

Solving Equations (9) and (10) yields the eigenfrequencies  $\omega_i$  and eigenvectors  $\{u_{\tilde{n}}\}$  of each order modes, which respectively correspond to the natural frequencies and modal modes of the vibration system. The SRM can be simplified to a second-order system, and its input and output are the radial force  $F_r$  and the motor surface displacement  $x$ , respectively. The motor surface displacement is the displacement of the measuring point, which is located on the outer surface of the stator core and directly above the salient pole of any phase (e.g., phase A), as shown in Figure 4. The generic modal superposition method [25] is used to predict the system output  $x$ , namely

$$x(s) = \sum_{i=1}^n Q_i \frac{1}{s^2 \zeta_i \omega_{ni} s + \omega_{ni}^2}, \quad (11)$$

where  $\omega_{ni}$  is the characteristic frequency,  $\zeta_i = c/2m\omega_n$  is the damping ratio, and  $Q_i$  is the gain coefficient of the  $i_{th}$  order mode.

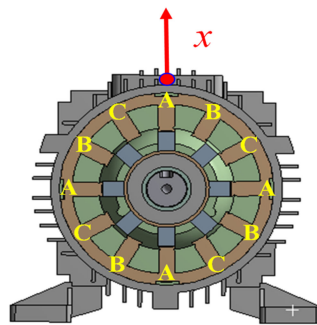


Figure 4. Illustration of the motor surface displacement.

## 4. Experimental Results and Verification

### 4.1. Implementation of Simulated and Experimental Platforms

The implementation of the vibration prediction model based on the multi-physics analysis is illustrated in Figure 5. The controller is built with MATLAB/Simulink (R2017a, the MathWorks, Inc., Natick, MA, USA). The information exchange between controller and drive circuit is realized by S-Function. The speed control module is constructed by the existing module of Simulink. The current control module, i.e., the drive circuit switch control module, is programmed using the S-Function. The modeling circuit of the driver circuit module is the same as the actual driver circuit that consists of IGBT. In addition, the inductance and resistance of the driver circuit are added to the model to simulate the characteristics of the real circuit. The drive circuit model of SRM is built by the ANSYS Simplorer (19.0.0, ANSYS, Inc., Canonsburg, PA, USA) and the mechanical module is established by the ANSYS Structure. The digital controller determines the gate signal generated by the driver circuit controller, and the power amplifier is driven by controlling the switch of the Insulated Gate Bipolar Transistor (IGBT). Consequently, an excitation current is generated in the field winding to form an electromagnetic field. Radial and tangential components of the electromagnetic force are then transmitted to the mechanical structure for vibration prediction. It is worth noting that the computing time for the multi-physics simulation depends on the running time we set. On average, it takes about 18 h and 30 min to accomplish the entire simulation process of 0.2 s on a workstation computer (Intel Xeon E5-1650 3.5 GHz, 64.0 GB of DDR3L RAM, Intel, Inc., Santa Clara, CA, USA, Windows 10 OS, Microsoft, Inc., Redmond, WA, USA).

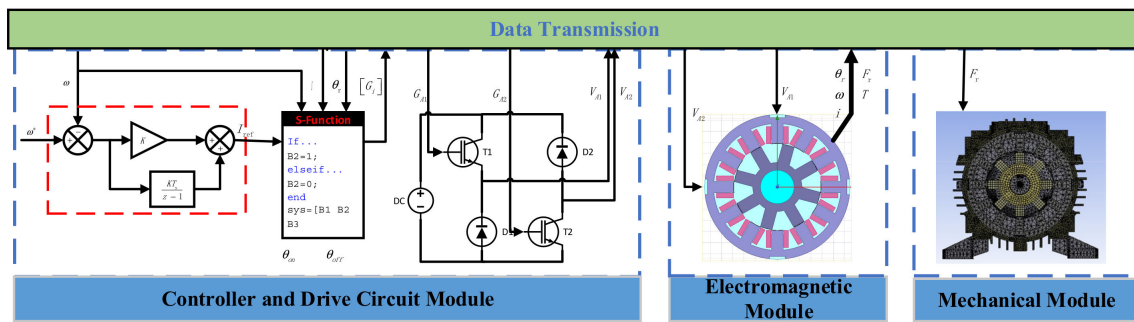


Figure 5. Schematic diagram of the simulation platform.

In general, electromagnetic field simulation of SRMs uses a two-dimensional model. The two-dimensional model ignores the edge effect of the motor, and the accuracy of the simulation results is slightly reduced compared to the three-dimensional model [31]. However, the computational efficiency of the two-dimensional model can be greatly improved compared with that of the three-dimensional model [32]. Therefore, electromagnetic field simulation is conducted with the two-dimensional model in this paper. In the two-dimensional simulation of electromagnetic field, it is assumed that the magnetic field is uniformly distributed along the axis. Meanwhile, the effects of end magnetic field and external magnetic field on the motor are neglected, and the stator outer ring is set as the simulation boundary. The main parameters of the SRM in this simulation is shown in Table 1, and the corresponding material parameters are listed in Table 2. Both stator and rotor of the SRM are laminated by the silicon steel sheet (Grade 50W470). The shaft material is 10# steel, while the winding material is copper. The stator, rotor and shaft of the SRM are modeled in the software and their material are set accordingly. Subsequently, the gap between the stator and rotor is modeled and its material is set to be air. Eventually, electromagnetic field simulation model can be established, as shown in Figure 6.

Table 1. Main dimension parameters of the model.

Name	Value	Name	Value	Name	Value
Stator Pole Number	12	Rotor Pole Number	8	Coil number	100
Stator outer diameter	130 mm	Rotor outer diameter	77.4 mm	Lamination coefficient	0.95
Stator inner diameter	78 mm	Rotor inner diameter	30 mm	Rotor pole arc coefficient	0.355
Stator yoke height	8 mm	Winding diameter	1.2 mm	Winding parallel number	2
Core length	120 mm	Rotor yoke height	7 mm	Stator pole arc coefficient	0.5

Table 2. Material parameters setup in finite element analysis (FEA).

Material	Density (kg/m <sup>3</sup> )	Poisson's Ratio	Young's Modulus (Pa)	Shear Modulus (Pa)
Silicon Steel	7700	0.26	$2 \times 10^{11}$	$7.9365 \times 10^{10}$
Gray Cast Iron	7200	0.28	$1.1 \times 10^{11}$	$4.2969 \times 10^{10}$
Structure steel	7850	0.30	$2 \times 10^{11}$	$7.6923 \times 10^{10}$
GCr15	7830	0.30	$2.19 \times 10^{11}$	$8.4200 \times 10^{10}$

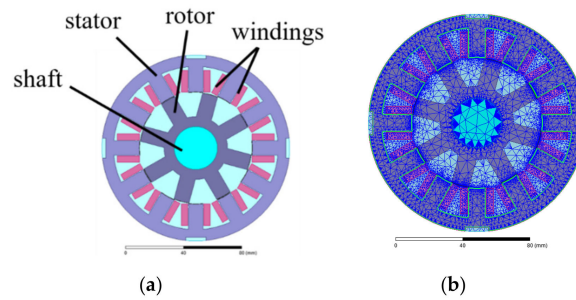


Figure 6. Electromagnetic field model: (a) structure (b) mesh.

In order to accurately model the structure of the SRM in Figure 1a, the constraints between the components are determined according to their real assembly arrangements. The modeling methods for individual components of the SRM are as follows.

The motor frame is fixed to the workbench through bolts, and the actual installation is completed by the constraints of the bolt holes and the frame surface. Considering the end cover and motor frame fixed to each other, they are handled as an integration. The stator is pressed into the casing through a pressing machine and is integrated with the frame. In addition, the stator is fixed to the motor frame. The winding is fixed to the stator slot by insulating sheets, which has a great influence on the stator mode and cannot be ignored. The equivalent effect of the windings is explored by changing the density of the stator material:

$$\tilde{\rho}_s = \frac{\rho_s V_s + \rho_c V_W}{V_s}, \tag{12}$$

where  $\tilde{\rho}_s$  is the equivalent stator density,  $\rho_s$  is the stator density (the density of silicon steel sheet),  $V_s$  is the stator volume,  $\rho_c$  is the winding density (copper wire density), and  $V_W$  is the winding volume.

Due to interference fit, the rotor and shaft are fixed to each other. The shaft is fixed to the inner ring of the bearings and thus it remains stationary between the front and rear end covers. The outer rings of both bearings are bonded to the front and rear end covers, and the friction coefficients between the inner and outer rings are set to be 0.0015.

Figure 7a shows the mechanical structure of the SRM and Figure 7b presents its meshing model. In the mechanical module, it not only includes the influence of the stator (containing iron core, winding, slot wedge, insulating material, and motor lead), but also fully considers the influence of rotor (containing rotor shaft and rotor core), end cover, bearing, and other structural components of the motor on the system modal. Meanwhile, the boundary conditions are set as the constraint of the movement and rotation of the base of the machine. Based on the simulation results and experimental data, the material parameters are adjusted to make the mass of the simulation mechanical model consistent with the actual mass of SRM. In addition, the model is tuned many times according to experimental results.

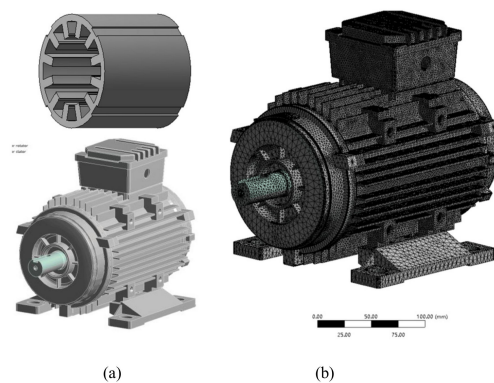
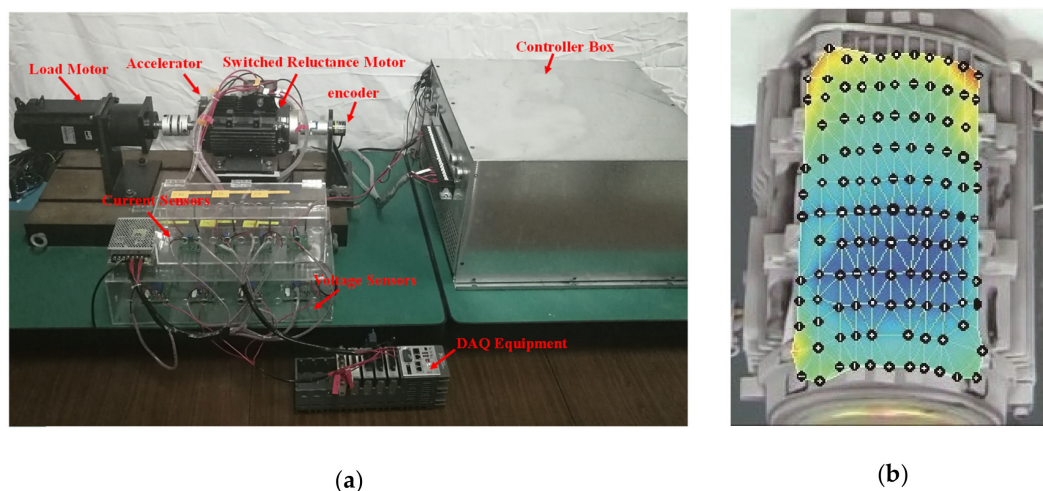


Figure 7. Three-dimensional structure of SRM and its meshing model: (a) mechanical structure of the SRM; (b) meshing model of the SRM.

To verify the effectiveness of the proposed multi-physics modeling-based method, a 1.5 kW SRM prototype with the same geometric parameters as the simulation model is utilized to build the experimental platform, as shown in Figure 8. The control of SRM is implemented in a Digital Signal Processor (DSP) TMS320F2812 from Texas Instruments (Dallas, TX, USA), which work at a frequency of 150 MHz. The current and voltage signals are measured in real time through sensors and data acquisition card. The rotor position is obtained by an incremental encoder with resolution of 1024. Meanwhile, the vibration is measured using a piezoelectric accelerometer attached to the housing surface of the stator core on the radial direction of the A-phase tooth as shown in Figure 8. Therefore, the measured shell surface vibration can reflect the actual vibration of the motor to the greatest extent. A 1.5 kW DC motor is used as the mechanical load and can provide a loading ranging from 0 to 20 Nm.



**Figure 8.** (a) The experimental platform of SRM; (b) the measurement points.

## 4.2. Simulation and Experimental Results

### 4.2.1. Analysis of Flux Linkage Characteristics

Based on the established magnetic field module, the flux linkage characteristics of several rotor angles are analyzed. Considering the accuracy of the position sensor used in the experimental test, the rotor angle is set from  $0^\circ$  (aligned position) to  $22.5^\circ$  (unaligned position) with the step increment of  $4.5^\circ$ . In the Ansys software (Canonsburg, PA, USA), the mesh can be divided intelligently. As can be seen from Figure 6b, the mesh around the air gap is finer. The excitation current is applied to phase A windings, and the value is between 2A and 16A, with the increment of 2A. The current density  $J_z$  is obtained by dividing the excitation current and the cross-sectional area of the winding wire. The magnetic vector distribution is solved by the software solver. The flux linkage data can be obtained after post-processing. To verify the simulation results, relevant experiments are carried out. The test procedure is as follows: fix the rotor at the required position, and apply a certain width pulse voltage to the A phase to make the current rise to at least 16A, then record the current and voltage data; tune the rotor to 4.5 degrees, repeat the previous operation until the rotor angle is 22.5 degrees, and then finish the measurement.

The comparison between the simulation results and experimental results is shown in Figure 9. It is seen that the flux linkage curve calculated by the simulated magnetic field is consistent with the experiment results, which proves that the magnetic field simulation model of the SRM built in this paper conforms to the characteristics of the actual motor. Meanwhile, Figure 9 shows that the flux linkage curve of the SRM is nonlinear, which is related to the rotor angle and current magnitude. When the rotor is at the aligned position, the flux linkage is the largest, while the flux linkage is smallest at the unaligned position. Due to the saturation characteristics of ferromagnetic material, the flux linkage begins to saturate when the current reaches to 6A. In addition, the simulated flux linkage curve agrees

well with the experimental curve in the rotor position region with smaller flux linkage, but there are some differences at the regions with larger flux linkage. The difference is manifested in the fact that the saturation effect of the flux linkage is greater in the experimental measured curve, that is, the slope of the relationship curve decreases faster.

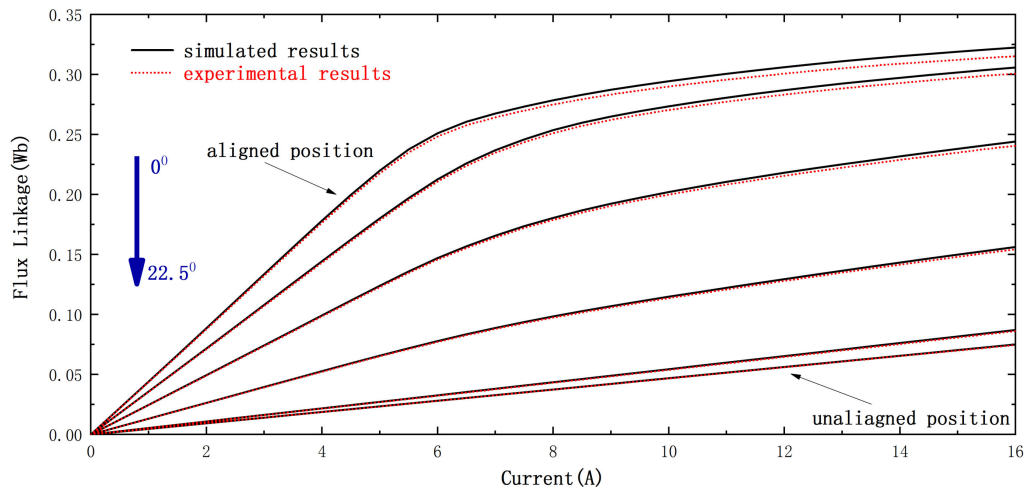


Figure 9. Flux linkage curve.

#### 4.2.2. Comparisons of the Obtained System Modal Results

The system modal of the SRM is obtained by using the simulation method presented in Section 3.3. In addition, the sinusoidal excitation method is adopted to acquire the actual system modal. Specifically, by applying different frequencies of sinusoidal signals to the SRM through exciter, the frequency response characteristics of the motor are obtained, and the vibration characteristics of the motor are determined. In the test, the SRM is fixed on the desktop by elastic cotton, and the sinusoidal excitation force is generated by the exciter (BK 4809, 10N). In addition, the vibration of the shell surface is recorded and analyzed by the laser Doppler Vibrometer (Polytech PSV-500-3D). Then, the exciter generates sinusoidal excitation with varying frequencies and scans the vibration response of the motor. The frequency response of the test points is shown in Figure 10. It is seen that the frequency of the first four orders are 618 Hz, 1215 Hz, 3022 Hz, 3856 Hz, respectively. The experimental characteristic frequencies are compared with those obtained by the proposed finite element method, as shown in Table 3. According to the simulation and experimental results, it is shown that the proposed modal simulation method based on static pre-calculation achieves high accuracy, and the errors between predicted and experimental results are within 3.7%. Compared with the results predicted by only considering the stator, the prediction error of the proposed method is reduced by at least 2.5%.

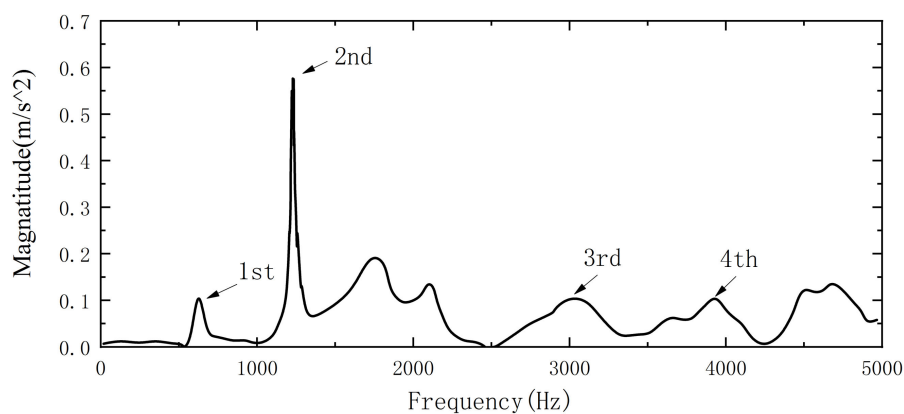


Figure 10. Frequency domain responses at the test point.

**Table 3.** Natural frequency results of FEA and the experimental method.

Mode Order	Experiment (Hz)	The Proposed FEA Method		FEA Considering Stator Only	
		Predicted Frequency (Hz)	Error (%)	Predicted Frequency (Hz)	Error (%)
1	618	602	2.59	583	5.66
2	1215	1198	1.40	1167	3.91
3	3022	2966	1.85	2885	4.53
4	3856	3999	3.70	3601	6.61

#### 4.2.3. Verification of the Vibration Prediction Model

In order to verify the accuracy of the vibration predictive model, the SRM operates under the condition of constant torque and speed. Vibration tests were carried out both on the simulation platform and experimental setup. The drive circuit adopted asymmetric half-bridge power amplifier. The speed controller adopted a proportional integral (PI) control algorithm, and the current controller used the hysteresis control method. To begin with, the speed was set as 625 rpm and the load torque was 2.5 Nm. For the sake of simplicity, the turn-on angle and turn off angle were chosen as 40° and 160° according to [33]. In addition, the damping coefficient is determined by measuring the attenuation speed of the motor vibration amplitude after the excitation stops, and the gain of the corresponding mode is calculated according to the measured damping coefficient. The obtained parameters for the vibration prediction model are shown in Table 4.

**Table 4.** Transfer function parameters for Modal 1–4 orders.

Mode Order	Frequency	Damping Ratio	Gain
1	602	0.0109	0.0000453
2	1198	0.0156	0.0000376
3	2966	0.0167	0.0000013
4	3999	0.0172	0.0000292

Since the electromagnetic force acting on the stator is directly related to the phase current, it is essential to accurately predict the current waveform. Figure 11a shows the comparison between the obtained current from the vibration prediction model and experimental results. The vibration spectrum obtained by experiment and simulation is shown in Figure 11b. It can be seen from the current curve that the experimental current value is not zero at the current turn-off point due to the zero drift of the current sensor. Although the simulation data and experimental data do not completely match because of the signal interference of the experimental platform itself, the error of current is relatively small and within an acceptable range. Simultaneously, based on Figure 11b, it can be seen from the vibration spectrum curve that the error of vibration magnitude is small, which validated the effectiveness of the proposed multi-physics modeling-based vibration prediction method.

Then, the speed was set as 1500 rpm and the load torque was 6.0 Nm. The turn-on angle and turn off angle were also chosen as 40° and 160°. Figure 12a presents the comparison between the obtained current from the vibration prediction model and experimental results for this case. The vibration spectrum obtained by experiment and simulation is illustrated in Figure 12b. It can be seen that, with the increase of speed and torque, the errors between the predicted values and the experimental results were still within the acceptable range. Consequently, the presented vibration prediction method based on multi-physical modeling can be utilized for the structural design optimization and control strategy optimization of SRMs.

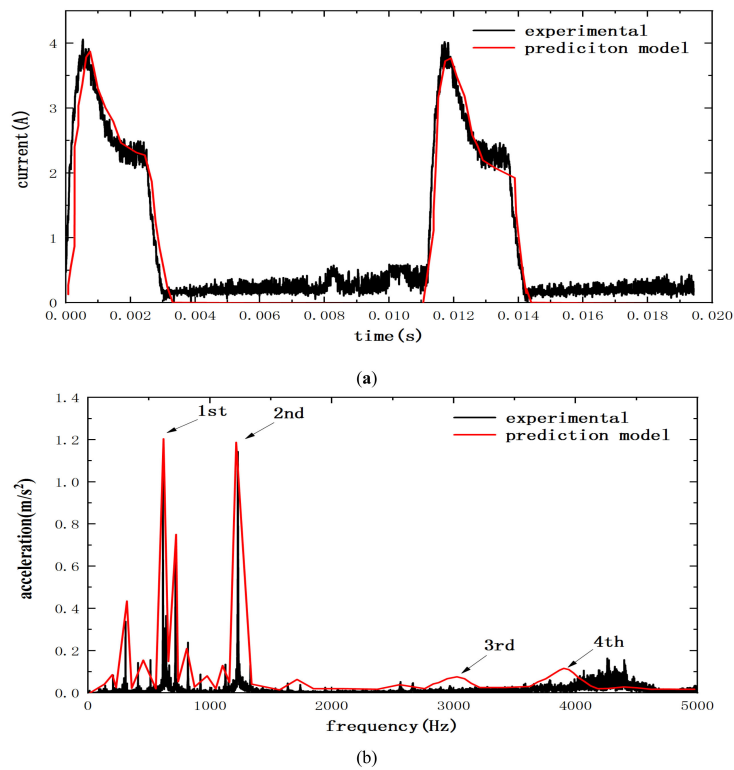


**Figure 11.** Current and vibration spectrum under simulated and experimental platform with the speed 625 rpm and the load torque 2.5 Nm: (a) current and (b) vibration spectrum.

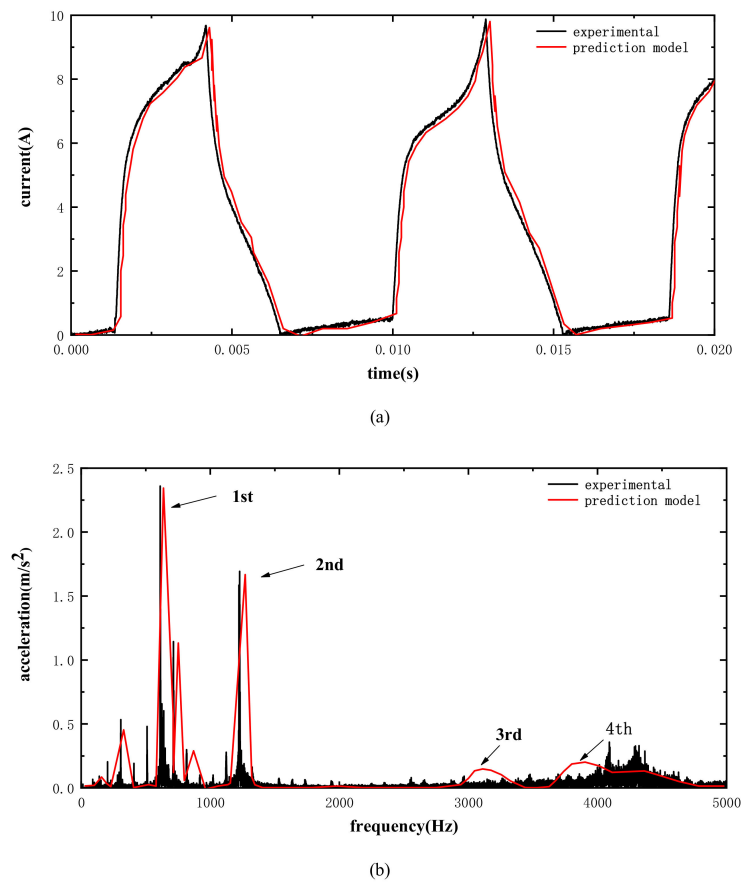


**Figure 12.** Current and vibration spectrum under simulated and experimental platform with the speed 1500 rpm and the load torque 6.0 Nm: (a) current and (b) vibration spectrum.

## 5. Conclusions

In this work, we develop a novel multi-physics modeling-based vibration prediction framework for SRM, in which the influence of components including stator, rotor, shell winding, end cover, and bearing on the system modal and interaction relationship of multi-physical field are fully taken into account. Through the integration of the control algorithm and the electromagnetic field analysis, the dynamic distribution of the electromagnetic field can be obtained to calculate the radial force. In the modal analysis, the influence of the stator, rotor, end cover, bearing and other components of the motor is fully considered. In addition, data dynamic interaction can be realized between the three segments, and the vibration data under different control strategies can be acquired in real time. To verify the proposed multi-physics modeling-based method, comparisons between the numerical and experimental results have been made. It is shown that the proposed vibration prediction method is provided with a high prediction accuracy for SRMs. Compared with the experimental results, the predicted error of vibration magnitude is quite small. Meanwhile, due to consideration of more components, the obtained system modal by the proposed method is rather accurate and the errors between predicted and experimental results are within 3.7%. Therefore, the proposed multi-physics modeling-based vibration prediction method can be applied to the structural design optimization and control strategy optimization of SRMs.

**Author Contributions:** Conceptualization, X.L. and J.T.; Data curation, X.L., B.L., and C.Q.; Formal analysis, X.L. and J.T.; Funding acquisition, C.L.; Investigation, J.T.; Methodology, X.K., J.T., B.L., and C.Q.; Project administration, C.L.; Resources, X.L. and J.T.; Supervision, C.L.; Validation, X.L., J.T., B.L., and C.Q.; Visualization, C.L.; Writing—original draft, X.L. and J.T.; Writing—review and editing, J.T. and C.L.

**Funding:** This research was funded by the National Natural Science Foundation of China (NSFC) (Grant No. 51935007 and No. 11202125 and No. 51305258).

**Conflicts of Interest:** The authors declare no conflict of interest.

## References

1. Gan, C.; Wu, J.; Sun, Q.; Kong, W.; Li, H.; Hu, Y. A Review on Machine Topologies and Control Techniques for Low-Noise Switched Reluctance Motors in Electric Vehicle Applications. *IEEE Access* **2018**, *6*, 31430–31443. [[CrossRef](#)]
2. Takeno, M.; Chiba, A.; Hoshi, N.; Ogasawara, S.; Takemoto, M.; Rahman, M.A. Test Results and Torque Improvement of the 50-kW Switched Reluctance Motor Designed for Hybrid Electric Vehicles. *IEEE Trans. Ind. Appl.* **2012**, *48*, 1327–1334. [[CrossRef](#)]
3. Bostanci, E.; Moallem, M.; Parsapour, A.; Fahimi, B. Opportunities and challenges of switched reluctance motor drives for electric propulsion: A comparative study. *IEEE Trans. Transp. Electrification* **2017**, *3*, 58–75. [[CrossRef](#)]
4. Yang, Z.; Shang, F.; Brown, I.P.; Krishnamurthy, M. Comparative Study of Interior Permanent Magnet, Induction, and Switched Reluctance Motor Drives for EV and HEV Applications. *IEEE Trans. Transp. Electrification* **2015**, *1*, 245–254. [[CrossRef](#)]
5. Sun, W.; Li, Y.; Huang, J.; Zhang, N. Vibration effect and control of In-Wheel Switched Reluctance Motor for electric vehicle. *J. Sound Vib.* **2015**, *338*, 105–120. [[CrossRef](#)]
6. Qin, Y.; He, C.; Shao, X.; Du, H.; Xiang, C.; Dong, M. Vibration mitigation for in-wheel switched reluctance motor driven electric vehicle with dynamic vibration absorbing structures. *J. Sound Vib.* **2018**, *419*, 249–267. [[CrossRef](#)]
7. Gan, C.; Wu, J.; Shen, M.; Yang, S.; Hu, Y.; Cao, W. Investigation of Skewing Effects on the Vibration Reduction of Three-Phase Switched Reluctance Motors. *IEEE Trans. Magn.* **2015**, *51*, 1–9. [[CrossRef](#)]
8. Widmer, J.D.; Mecrow, B.C. Optimized Segmental Rotor Switched Reluctance Machines with a Greater Number of Rotor Segments Than Stator Slots. *IEEE Trans. Ind. Appl.* **2013**, *49*, 1491–1498. [[CrossRef](#)]
9. Kurihara, N.; Bayless, J.; Sugimoto, H.; Chiba, A. Noise Reduction of Switched Reluctance Motor with High Number of Poles by Novel Simplified Current Waveform at Low Speed and Low Torque Region. *IEEE Trans. Ind. Appl.* **2016**, *52*, 3013–3021. [[CrossRef](#)]

10. Chai, J.Y.; Lin, Y.W.; Liaw, C.M. Comparative study of switching controls in vibration and acoustic noise reductions for switched reluctance motor. *IEE Proc. Electr. Power Appl.* **2006**, *153*, 348–360. [[CrossRef](#)]
11. Zhu, Z.Q.; Liu, X.; Pan, Z. Analytical Model for Predicting Maximum Reduction Levels of Vibration and Noise in Switched Reluctance Machine by Active Vibration Cancellation. *IEEE Trans. Energy Convers.* **2011**, *26*, 36–45. [[CrossRef](#)]
12. Takiguchi, M.; Sugimoto, H.; Kurihara, N.; Chiba, A. Acoustic Noise and Vibration Reduction of SRM by Elimination of Third Harmonic Component in Sum of Radial Forces. *IEEE Trans. Energy Convers.* **2015**, *30*, 883–891. [[CrossRef](#)]
13. Cai, W.; Pillay, P.; Tang, Z.; Omekanda, A.M. Low-vibration design of switched reluctance motors for automotive applications using modal analysis. *IEEE Trans. Ind. Appl.* **2003**, *39*, 971–977. [[CrossRef](#)]
14. Callegaro, A.D.; Liang, J.; Jiang, J.W.; Bilgin, B.; Emadi, A. Radial Force Density Analysis of Switched Reluctance Machines: The Source of Acoustic Noise. *IEEE Trans. Transp. Electrification* **2019**, *5*, 93–106. [[CrossRef](#)]
15. Kimpara, M.; Wang, S.; Reis, R.; Pinto, J.; Moallem, M.; Fahimi, B. On the Cross Coupling Effects in Structural Response of Switched Reluctance Motor Drives. *IEEE Trans. Energy Convers.* **2019**, *34*, 620–630. [[CrossRef](#)]
16. Liang, X.; Li, G.; Ojeda, J.; Gabsi, M.; Ren, Z. Comparative Study of Classical and Mutually Coupled Switched Reluctance Motors Using Multiphysics Finite-Element Modeling. *IEEE Trans. Ind. Electron.* **2014**, *61*, 5066–5074. [[CrossRef](#)]
17. Li, J.; Cho, Y. Investigation into Reduction of Vibration and Acoustic Noise in Switched Reluctance Motors in Radial Force Excitation and Frame Transfer Function Aspects. *IEEE Trans. Magn.* **2009**, *45*, 4664–4667.
18. Cameron, D.E.; Lang, J.H.; Umans, S.D. The origin and reduction of acoustic noise in doubly salient variable-reluctance motors. *IEEE Trans. Ind. Appl.* **1992**, *28*, 1250–1255. [[CrossRef](#)]
19. Anwar, M.N.; Husain, O. Radial force calculation and acoustic noise prediction in switched reluctance machines. *IEEE Trans. Ind. Appl.* **2000**, *36*, 1589–1597.
20. Husain, A.R.; Nairus, J. Unbalanced force calculation in switched-reluctance machines. *IEEE Trans. Magn.* **2000**, *36*, 330–338. [[CrossRef](#)]
21. Bracikowski, N.; Hecquet, M.; Brochet, P.; Shirinskii, S.V. Multiphysics Modeling of a Permanent Magnet Synchronous Machine by Using Lumped Models. *IEEE Trans. Ind. Electron.* **2012**, *59*, 2426–2437. [[CrossRef](#)]
22. Le Besnerais, J.; Fasquelle, A.; Hecquet, M.; Pelle, J.; Lanfranchi, V.; Harmand, S. Multiphysics Modeling: Electro-Vibro-Acoustics and Heat Transfer of PWM-Fed Induction Machines. *IEEE Trans. Ind. Electron.* **2010**, *57*, 1279–1287. [[CrossRef](#)]
23. Fiedler, O.; Kasper, K.A.; De Doncker, R.W. Calculation of the Acoustic Noise Spectrum of SRM Using Modal Superposition. *IEEE Trans. Ind. Electron.* **2010**, *57*, 2939–2945. [[CrossRef](#)]
24. Srinivas, N.; Arumugam, R. Analysis and characterization of switched reluctance motors: Part II. Flow, thermal, and vibration analyses. *IEEE Trans. Magn.* **2005**, *41*, 1321–1332. [[CrossRef](#)]
25. Tang, Z.; Pillay, P.; Omekanda, A.M. Vibration prediction in switched reluctance motors with transfer function identification from shaker and force hammer tests. *IEEE Trans. Ind. Appl.* **2003**, *39*, 978–985. [[CrossRef](#)]
26. Lin, C.; Fahimi, B. Prediction of Radial Vibration in Switched Reluctance Machines. *IEEE Trans. Energy Convers.* **2013**, *28*, 1072–1081. [[CrossRef](#)]
27. Guo, X.; Zhong, R.; Zhang, M.; Ding, D.; Sun, W. Fast Computation of Radial Vibration in Switched Reluctance Motors. *IEEE Trans. Ind. Electron.* **2018**, *65*, 4588–4598. [[CrossRef](#)]
28. Arumugam, R.; Lowther, D.; Krishnan, R.; Lindsay, J. Magnetic field analysis of a switched reluctance motor using a two dimensional finite element model. *IEEE Trans. Magn.* **1985**, *21*, 1883–1885. [[CrossRef](#)]
29. Parreira, B.; Rafael, S.; Pires, A.J.; Branco, P.J.C. Obtaining the magnetic characteristics of an 8/6 switched reluctance machine: From FEM analysis to the experimental tests. *IEEE Trans. Ind. Electron.* **2005**, *52*, 1635–1643. [[CrossRef](#)]
30. Bilgin, B.; Jiang, J.W.; Emadi, A. *Switched Reluctance Motor Drives: Fundamentals to Applications*, 1st ed.; CRC Press: Boca Raton, FL, USA, 2018.
31. Chen, H.; Nie, R.; Sun, M.; Deng, W.; Liang, K. 3-D Electromagnetic Analysis of Single-Phase Tubular Switched Reluctance Linear Launcher. *IEEE Trans. Plasma Sci.* **2017**, *45*, 1553–1560. [[CrossRef](#)]

32. Deshpande, U. Two-dimensional finite-element analysis of a high-force-density linear switched reluctance machine including three-dimensional effects. *IEEE Trans. Ind. Appl.* **2000**, *36*, 1047–1052. [[CrossRef](#)]
33. Ye, J.; Malysz, P.; Emadi, A. A Fixed-Switching-Frequency Integral Sliding Mode Current Controller for Switched Reluctance Motor Drives. *IEEE J. Emerg. Sel. Top. Power Electron.* **2015**, *3*, 381–394.



© 2019 by the authors. Licensee MDPI, Basel, Switzerland. This article is an open access article distributed under the terms and conditions of the Creative Commons Attribution (CC BY) license (<http://creativecommons.org/licenses/by/4.0/>).